David E. Huber[1]
Juan G. Santiago[2]

[1]Microfluidics Department, Sandia National Laboratories, Livermore, CA, USA
[2]Department of Mechanical Engineering, Stanford University, Stanford, CA, USA

Received July 27, 2006
Revised December 19, 2006
Accepted January 5, 2007

Research Article

Taylor–Aris dispersion in temperature gradient focusing

Microfluidic temperature gradient focusing (TGF) uses an axial temperature gradient to induce a gradient in electrophoretic flux within a microchannel. When balanced with an opposing fluid flow, charged analytes simultaneously focus and separate according to their electrophoretic mobilities. We present a theoretical and experimental study of dispersion in TGF. We model the system using generalized dispersion analysis that yields a 1-D convection-diffusion equation that contains dispersion terms particular to TGF. We consider analytical solutions for the model under uniform temperature gradient conditions. Using a custom TGF experimental setup, we compare focusing measurements with the theoretical predictions. We find that the theory well represents the focusing behavior for flows within the Taylor–Aris dispersion regime.

Keywords:
Dispersion / Microfluidics / Preconcentration / Taylor–Aris / Temperature gradient focusing
DOI 10.1002/elps.200600830

1 Introduction

Over the last decade, microfluidics technology has contributed to the development of many miniaturized bioanalytical techniques, in pursuit of the goal of the micro total analysis system (μTAS) or "lab-on-a-chip" system [1–3]. Miniaturization can yield significant performance improvements in speed, reagent consumption, and integration capability. However, the development of robust, highly sensitive on-chip assays still poses significant challenges. For this reason, on-chip preconcentration techniques are of great interest to the microfluidics community. Examples include field-amplified sample stacking [4, 5], micellar sweeping [6], and IEF [7]. Microfluidic temperature gradient focusing (TGF) [8] is a promising assay that simultaneously concentrates and separates charged species according to their electrophoretic mobilities. TGF can be classified as a type of electric field gradient focusing [9].

The capabilities of TGF allow it to be used in analytical (*i.e.*, detection and separation) and preparative (*i.e.*, concentration and purification) applications. For both types of applications, an important design goal is the minimization of the physical phenomena that cause band broadening, which fall under the general term "dispersion". Decreasing dispersion improves resolution and sensitivity in separation applications [10], and also yields improved dynamics for concentration and purification applications [11].

One of the first detailed studies of dispersion in pressure-driven channel flow was published by Taylor in 1953 [12]. He showed that, under fairly general conditions, the cross-sectional average of the unsteady, 3-D concentration field evolves as a 1-D convection-diffusion equation, where the diffusion coefficient, D, is replaced with an effective dispersion constant. The concept has proved to be extremely useful and has been extended to other flow regimes [13] and geometries [14]. Alternative analyses have generalized the approach [15, 16], and in the field of microfluidics, the analysis has been applied to electroosmotic flows [17] and electrophoresis in nanochannels [18]. TGF is relatively new and no analysis of TGF dispersion has been presented.

Microfluidic TGF was first demonstrated by Ross and Locascio [8]. Using a buffer which demonstrates a temperature-dependent ionic strength (*e.g.*, due to temperature-dependent dissociation of a weak electrolyte), they successfully focused charged fluorescent dyes, amino acids, green fluorescent protein, DNA, and polystyrene particles, illustrating the general applicability of TGF. TGF has subsequently been extended to DNA hybridization assays and SNP detection [19], as well as the detection of chiral enantiomers [20]. Focusing of neutral and ionic hydrophobic analytes has also been achieved [21] using TGF combined with micellar EKC [6].

Correspondence: Dr. David E. Huber, Sandia National Laboratories, Microfluidics Department, P.O. Box 969, MS 9292, Livermore, CA 94551-0969, USA
E-mail: dhuber@sandia.gov
Fax: +1-925-294-3020

Abbreviations: RTD, resistance temperature detector; **TGF,** temperature gradient focusing

In this work, we develop a dispersion theory for focusing systems and compare with results from our TGF experiments. The paper is organized as follows, we first review the basic theory relevant to TGF. Then we develop our general dispersion theory, which comprises a lubrication solution for the flow field, a generalized dispersion analysis yielding a Taylor-like dispersion equation, and simplified analytical solutions for the shape of focused peaks. Finally, we describe our experimental results, beginning with our calibration experiments and concluding with our focusing results.

2 TGF theory

In TGF, a temperature gradient is applied axially along an electrophoretic channel. Within the channel, the local electric field is inversely proportional to conductivity [8], which in turn is a function of local viscosity and ion density. By selecting a buffer with a temperature-dependent conductivity, we create an electric field gradient that causes a decrease in electrophoretic mass flux along one direction in the channel. We then impose a net bulk flow in the opposite direction (see Fig. 1), through a combination of EOF and pressure-driven flow. As we shall discuss below, charged species focus at points where local fluxes associated with area-averaged liquid velocity, $\bar{u}_{\mathrm{bulk}}$, electrophoretic velocity, $\bar{u}_{\mathrm{eph}}$, and a "diffusive velocity" term (*i.e.*, a net drift in species associated with the gradient of diffusivity) of the form $-\mathrm{d}\bar{D}/\mathrm{d}x$ sum to zero. Here, D is the diffusivity, x is the axial direction, and the overbars indicate the cross-section average.

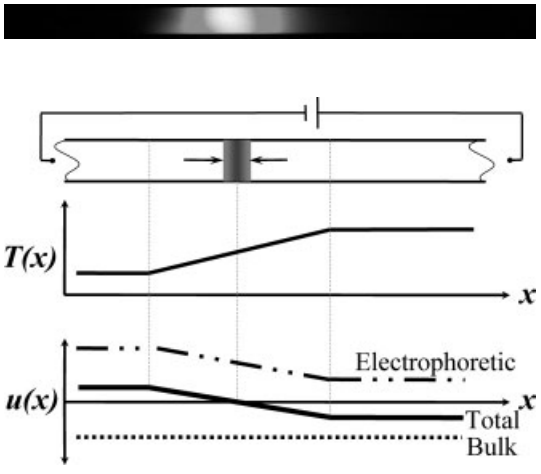

Figure 1. Scheme of TGF process (after Fig. 1 of Ross and Locascio [8]). A temperature gradient is applied to a microchannel which induces a gradient in the electrophoretic velocity of an analyte. A counterflow of liquid opposes the electrophoretic flux. The analyte focuses at the point where the electrophoretic and convective fluxes sum to zero. Both molecular diffusion and advective dispersion contribute to the broadening of the band about the focus point. The top image shows 50-fold focused Bodipy in an applied electric field of 40 V/mm within a 20×200 μm wide channel.

We leverage the net neutrality approximation [22] and use Ohm's law to determine the local electric field, and write the electrophoretic velocity as

$$\mathbf{u}_{\mathrm{eph}} = \nu_{\mathrm{eph}}\mathbf{E} = \nu_{\mathrm{eph}}\mathbf{i}/\sigma \tag{1}$$

where ν_{eph} is the electrophoretic mobility, $\mathbf{E}$ the electric field, $\mathbf{i}$ the current flux, and σ the conductivity. In further analyzing the behavior of TGF, we adopt the convention of Ross and Locascio, [8] and write the conductivity as $\sigma(T) = \mu_0\sigma_0/(\mu f)$, where μ_0 and σ_0 are the buffer viscosity and conductivity at a defined reference temperature, $\mu(T)$ is the viscosity, and $f(T)$ is a nondimensional function incorporating any remaining conductivity dependencies. (The parenthetic "T" is a reminder that these quantities are temperature-dependent.) A similar decomposition is applied to the electrophoretic mobility, such that $\nu_{\mathrm{eph}} = \nu_{0,\mathrm{eph}}\mu_0/(\mu f_{\mathrm{eph}})$ where $\nu_{0,\mathrm{eph}}$ is the analyte's electrophoretic mobility at the reference temperature, and $f_{\mathrm{eph}}(T)$ accounts for any other temperature dependencies. As pointed out by Ross and Locascio [8], the usefulness of this decomposition becomes apparent when we solve for the 1-D electrophoretic velocity (*i.e.*, in the case of uniform cross-sectional temperature). If we assume uniform current, I, and again use Ohm's law to calculate the local electric field, the axial electrophoretic velocity reduces to $u_{\mathrm{eph}} = \nu_{0,\mathrm{eph}}E_0 f/f_{\mathrm{eph}}$, where $E_0 = I/A\sigma_0$, and A is the channel cross-sectional area. In this work, we assume $f_{\mathrm{eph}}(T) = 1$, which is equivalent to saying the ion has constant charge and obeys a Stokes hard sphere drag model. In this case, we see that the electrophoretic velocity is a function only of the temperature, through f. Additionally, we note that the rate of mass accumulation due to electrophoretic focusing over a volume is proportional to the difference in f on the boundaries. However, for a differential volume, or for linear $f(T(x))$, the focusing is proportional to the slope of f.

3 Dispersion theory

We model our focusing system using a convection-diffusion equation incorporating a conservative electrophoretic flux term. In its most general form, we have

$$\frac{\partial c}{\partial t} + \mathbf{u}_{\mathrm{bulk}}\nabla c + \nabla(\mathbf{u}_{\mathrm{eph}}c) = \nabla\nabla(Dc) \tag{2}$$

where c is the concentration of our sample analyte and D is the analyte's molecular diffusivity. Note the placement of the diffusivity within the second gradient operator. This reflects the use of the Fokker–Planck diffusivity law, $\mathbf{J} = -\nabla(Dc)$. While it is common (albeit incorrect) practice to use Fick's law for the diffusive flux (yielding the traditional $\nabla\cdot D\nabla c$), Fick's law strictly applies only for homogeneous D [23]. To recover the more familiar diffusion representation, we can carry out the differentiation, which yields the terms, $D\nabla c$ and $c\nabla D$. The latter term thus represents a flux due to a diffusiv-

ity-induced velocity, ∇D, that we then move to the left-hand side of the equation and combine with the electrophoretic velocity.

We wish to simplify our general equation to gain insight into the dispersive characteristics of the system. Our goal is to generate analytical solutions that may be used for design guidance. In the following sections, we develop an analytical expression for the bulk velocity using the lubrication approximation, apply generalized dispersion theory to yield a 1-D convection-diffusion equation for TGF, then construct analytical solutions.

3.1 Velocity field

As in most microchannel systems, the Reynolds number is much less than unity and the Debye length is several orders of magnitude smaller than the characteristic dimensions of the channel. In contrast to typical systems, the axial temperature gradient induces conductivity and permittivity gradients in the channel, and these result in net charge in the bulk flow (*i.e.*, regions outside charged double layers) [24], but, for the length scales and temperature gradients of typical electrophoresis flow fields, the dispersion associated with these electric body forces can be neglected compared to dispersion caused by gradients in the wall zeta potential [11]. We can therefore assume that the bulk flow has no net charge and use a modified form of the Stokes equation, $0 = -\nabla p + \nabla\mu(\nabla \mathbf{u}_{\text{bulk}} + (\nabla \mathbf{u}_{\text{bulk}})^{\text{T}})$ to account for the varying viscosity. The nonuniform slip boundary condition is given by the Helmholtz–Smoluchowski relation of the form $u_{\text{eo}} = \nu_{\text{eo}} E = \varepsilon\zeta E/\mu$, where u_{eo} is the EOF velocity at the interface between the bulk and charge layer, ε is the permittivity, ζ the zeta potential, E the local axial electric field, and μ the local viscosity [25].

Extending the decomposition procedure described in Section 2 to the electroosmotic velocity, we find that we can write the local electroosmotic slip velocity as

$$u_{\text{eo}} = \nu_{\text{eo},0} E_0 f(T) g(T) \tag{3}$$

where we define $g(T) \equiv \nu_{\text{eo}}(T)\mu(T)/\nu_{\text{eo},0}\mu_0 = \varepsilon(T)\zeta(T)/\varepsilon_0\zeta_0$. Equation (3) is strictly applicable only when the buffer temperature and wall temperature are equal. If a significant wall-normal temperature gradient exists within the channel, g should be evaluated with the wall temperature, while f is evaluated with an area-averaged buffer temperature.

At this point, we limit our discussion to flow between two large parallel plates (although our approach can also be applied readily to flow in a cylindrical tube) and eliminate the z-dependence. To determine an analytical expression for the velocity field, we extend the lubrication flow solution of Ghosal [26] to include variable viscosity and the nonuniform electroosmotic slip velocity of Eq. (3). (For additional details on the derivation, see Appendix A.) This gives

$$u_{\text{bulk}}(x,y) = \left\{\frac{a^2}{2\langle\mu\rangle}\frac{\Delta P}{L_{\text{ch}}} + \frac{3}{2}\nu_{\text{eo},0}E_0\left(\frac{\langle\mu fg\rangle}{\langle\mu\rangle} - fg\right)\right\}\left(1 - \frac{y^2}{a^2}\right) + \nu_{\text{eo},0}E_0 fg \tag{4}$$

$$v_{\text{bulk}}(x,y) \approx 0 \tag{5}$$

where a is the channel half-height, L_{ch} the length of the channel, $\triangle P$ the applied pressure difference, and the angle brackets indicate an axial mean over the length of the channel. The flow field is a superposition of a uniform electroosmotic component and a parabolic (in y) pressure-driven component. These two are linked through continuity, so as one decreases, the other must increase. Thus, the pressure driven flow component (curved brackets) contains both the externally applied pressure gradient and the internally generated pressure gradient, which results from the local slip velocity deviating from the axial average. Note that the angle-bracketed terms are uniform and constant, and f and g are functions of T, so the velocity profile varies in x in response to axial temperature changes.

3.2 Generalized dispersion analysis

We now return to the general convection-diffusion equation, Eq. (2). To begin our generalized dispersion analysis, we decompose our variables into a cross-sectional area-averaged component and a deviation component, as suggested by the work of Stone and Brenner [16]. In Cartesian coordinates, the decomposed variables take the form $f = \bar{f}(x) + f'(x,y,z)$, where the overbar denotes the area-averaged value and the prime denotes the deviation component. The cross-sectional average is given by simply $\bar{f} = \left(\int f dA\right)/A$. (Note this is in contrast to the axial average used in the lubrication solution, which is denoted by $< >$.)

After decomposing the terms in Eq. (1), we perform the cross-sectional average of the full equation, thus eliminating products containing a single deviation term. (The average of a deviation term is zero, by definition.) This leaves several integral terms which are simplified by applying continuity ($\partial u'/\partial x + \partial v'/\partial y + \partial w'/\partial z = 0$) and the no-flux boundary conditions at the wall ($\partial c'/\partial n = 0$ where c' is the deviation concentration and n is the wall normal direction), yielding (in scalar form):

$$\frac{\partial \bar{c}}{\partial t} + \bar{u}_{\text{bulk}}\frac{\partial \bar{c}}{\partial x} + \frac{\partial}{\partial x}\left(\bar{u}_{\text{eph}}\bar{c} - \frac{\partial \bar{D}}{\partial x}\bar{c}\right) = = \frac{\partial}{\partial x}\left(\bar{D}\frac{\partial \bar{c}}{\partial x} + \frac{\partial}{\partial x}\overline{D'c'} - \overline{u'_{\text{bulk}}c'} - \overline{u'_{\text{eph}}c'}\right) \tag{6}$$

At this point, we note that no significantly limiting approximations have been made to the general problem. Equation (6) is the transport equation for the area-averaged concentration. It has the same form as the standard 1-D transport equation with the addition of three cross-correlation terms that contribute to the dispersion.

We now simplify Eq. (6) assuming an ideal temperature gradient system in which the temperature varies only in the axial dimension. In this case, although the molecular diffusivity and electrophoretic velocity are functions of temperature, D' and u'_{eph} both equal zero.

The remaining correlation term on the right-hand side, $\overline{u'_{\mathrm{bulk}}c'}$, corresponds to the advective dispersion arising from transverse variations in the axial velocity. To evaluate this, we require the transport equation for the deviation concentration, which is derived by subtracting Eq. (6) from the decomposed form of Eq. (2). We then apply the ideal (*i.e.*, uniform in y) temperature gradient simplification to obtain (for the full vector equation):

$$\frac{\partial c'}{\partial t} + \bar{\mathbf{u}}_{\mathrm{bulk}}\nabla c' + \mathbf{u}'_{\mathrm{bulk}}\nabla(\bar{c}+c') + \\ +\nabla(\bar{\mathbf{u}}_{\mathrm{eph}}c' - c'\nabla\bar{D}) = \nabla\cdot\bar{D}\nabla c' + \nabla\overline{\mathbf{u}'_{\mathrm{bulk}}c'} \quad (7)$$

We further simplify the deviation equation by invoking our parallel plates geometry and removing the z-dependence. We then eliminate terms using the following Taylor-analysis inspired scaling arguments [16] of the form

$$\bar{c} \gg c',\ \frac{L_{\mathrm{peak}}}{a} \gg \frac{U_{\mathrm{p}}a}{\bar{D}_0} \equiv Pe_{\mathrm{a}},$$
$$L_{\mathrm{grad}}, L_{\mathrm{peak}} \gg a,\ u'_{\mathrm{bulk}} = O(u_{\mathrm{bulk}}) \quad (8)$$

where the new terms are the area-averaged pressure-driven velocity (*i.e.*, neglecting the uniform contribution due to electroosmosis), U_{p}, the molecular diffusivity at the focus point, D_0, the pressure-driven Peclet number, Pe_a (defined as shown), the length of the temperature gradient region, L_{grad}, and the characteristic axial dimension of the peak, L_{peak}. Under these conditions, our system falls within the Taylor–Aris regime [13] for convective transport, and the deviation equation reduces to

$$u'_{\mathrm{bulk}}\frac{\partial\bar{c}}{\partial x} = \bar{D}\frac{\partial^2 c'}{\partial y^2} \quad (9)$$

(For further details on the scaling, see Appendix B.) We note that $\bar{D}$ and u'_{bulk} are both functions of x. Given an expression for u'_{bulk} we may then solve for c' in terms of $\bar{c}$. To yield u'_{bulk} we perform the area-averaged decomposition on the lubrication flow solution, Eq. (3), which gives

$$\bar{u}_{\mathrm{bulk}} = \frac{a^2}{3\langle\mu\rangle}\frac{\Delta P}{L_{\mathrm{ch}}} + \nu_{\mathrm{eo},0}E_0\frac{\langle\mu fg\rangle}{\langle\mu\rangle} \quad (10)$$

$$u'_{\mathrm{bulk}} = \left\{\frac{a^2}{3\langle\mu\rangle}\frac{\Delta P}{L_{\mathrm{ch}}} + \nu_{\mathrm{eo},0}E_0\frac{\langle\mu fg\rangle}{\langle\mu\rangle} - \nu_{\mathrm{eo},0}E_0 fg\right\}\left(\frac{1}{2} - \frac{3y^2}{2a^2}\right) \quad (11)$$

Here, the bracketed expression is the area-averaged value of the local pressure driven flow (U_{p}). Under equivalent focusing conditions (*i.e.*, same focus temperature and negligible Joule heating), $U_{\mathrm{p}} \sim E_0$ since the applied pressure gradient must also grow as E_0 to maintain the focusing criterion. Substituting Eq. (11) into Eq. (9), we can integrate to obtain c'. We may now determine the advective dispersion contribution.

$$\overline{u'_{\mathrm{bulk}}c'} = \frac{2}{105}\frac{U_{\mathrm{p}}^2a^2}{\bar{D}}\frac{\partial\bar{c}}{\partial x} = \frac{2\bar{D}}{105}Pe_{\mathrm{a}}^2\frac{\partial\bar{c}}{\partial x} \quad (12)$$

We substitute Eq. (12) into our cross-section averaged transport equation yielding its final form

$$\frac{\partial\bar{c}}{\partial t} + \bar{u}_{\mathrm{bulk}}\frac{\partial\bar{c}}{\partial x} + \frac{\partial}{\partial x}(\bar{u}_{\mathrm{eph}}\bar{c}) - \frac{\partial}{\partial x}\left(\frac{\partial\bar{D}}{\partial x}\bar{c}\right) = \frac{\partial}{\partial x}\left(D_{\mathrm{eff}}\frac{\partial\bar{c}}{\partial x}\right) \quad (13)$$

where

$$D_{\mathrm{eff}} = \bar{D}\left(1 + \frac{2}{105}Pe_{\mathrm{a}}^2\right) \quad (14)$$

Our 1-D convection-diffusion equation has features of the Taylor–Aris dispersion equation. However, in contrast to Taylor–Aris, D_{eff} is here a function of temperature and the axial coordinate, as it depends on both $\bar{D}$ and U_{p}. There is also a diffusive drift velocity due to the axial gradient of $\bar{D}$.

3.3 Extension to 3-D channels

While the parallel plates formulation used above is a rough approximation to 3-D channels, it is made here to simplify the derivation of the dispersion correlation. This analysis results in dispersion rate relations with the correct dependence on bulk velocity, channel depth, and molecular diffusivity. However, it neglects the dispersion associated with the sidewalls (channel walls parallel to the x–y plane). As noted by Ajdari *et al.* [27], to remain within the Taylor regime we must also satisfy $L_{\mathrm{peak}}/w >> Pe_w$, where w is the channel width. We can then account for the additional sidewall dispersion by multiplying our advective dispersion term (Eq. 12) with a factor given by the Chatwin solution for rectangular cross-section channels [28]. For the case of a 10:1 aspect ratio channel, the multiplier is approximately 7 [29]. The effective dispersion coefficient is then $D_{\mathrm{eff}} \cong \bar{D}(1 + 14\,Pe_{\mathrm{a}}^2/105)$.

In summary, our analysis is valid for the case of TGF in a long thin channel with thin electric double layers and negligible bulk charge. We also assume $Pe_a << L/a$, $Pe_w << L/w$, $a << L_{\mathrm{grad}}$, L_{peak}, and uniform temperature within a given cross-section. If any of these assumptions are violated, then new dispersion mechanisms may arise. For example, if Pe_a is of order L_{peak}/a, then ballistic dispersion [27] can become significant. While these restrictions seem limiting, we note that use of small channel cross-sections can ensure that all criteria are met.

3.4 Analytical solutions

We wish to develop analytical solutions for the 1-D cross-section averaged convection-diffusion equation, in order to understand the influence of dispersion on the shape of

focused sample bands. To do so, we begin with the quasi-steady approximation, which assumes that sufficient focusing has occurred, such that the rate of accumulation is small relative to the diffusive and electromigration fluxes. We can then eliminate the unsteady term in Eq. (13). Next, we eliminate the diffusive "velocity" term (which is small relative to the electrophoretic velocity) and integrate the quasi-steady state equation in x to yield the 1-D flux equation.

$$D_{\text{eff}}(T(x))\frac{\partial \bar{c}}{\partial x} = [\bar{u}_{\text{bulk}} + E_0 \nu_0 f(T(x))]\bar{c}(x) + C_1 \tag{15}$$

where C_1 is the constant of integration corresponding to the net species flux. At steady state, the net flux is zero. In practice, quasi-steady systems will experience some degree of net flux, since it is difficult to position a peak such that the flux from the left-hand side exactly balances the flux from the right-hand side. If we neglect the influence of this flux on the peak shape (and set $C_1 = 0$), we see that the solution has the form

$$c(x) = c_0 \exp\left[\int \frac{\bar{u}_{\text{bulk}} + E_0 \nu_0 f(T(x))}{D_{\text{eff}}(T(x))}\,\mathrm{d}x\right] \tag{16}$$

In general, since both the dispersion coefficient and f have a complex dependence on x, this equation may only be solved numerically. However, if we approximate D_{eff} and f with Taylor series expansions about the focus point, a variety of analytical solutions exist. For uniform effective diffusivity and linear $f = f_1 x + f_{\text{foc}}$ (*i.e.*, 0th and 1st order Taylor expansions), Ross and Locascio [8] determined that the solution to (Eq. 16) is a simple Gaussian with variance $\alpha^2 = -D_{\text{eff}}/E_0 \nu_0 f_1$, (at a stable focus point, $E_0 \nu_0 f_1 < 0$). (Also, see Ghosal and Horek [30] for a numerical solution of the unsteady equation using uniform D_{eff}.) To account for the spatial variation of dispersion, we also expand the effective dispersion coefficient to first order, giving $D_{\text{eff}} = D_1 x + D_{\text{foc}}$. We can then integrate Eq. (16) to obtain

$$c = c_0 \exp\left\{-\frac{\tilde{x}/L - \ln(1 + \tilde{x}/L)}{\alpha^2/L^2}\right\} \tag{17}$$

where $\tilde{x} = x - x_{\text{foc}}$, $L = D_{\text{foc}}/D_1$, and α^2 is $-D_{\text{foc}}/E_0 \nu_0 f_1$. Under this scaling, the solution collapses to a curve whose shape is determined by α/L, as shown in Fig. 2. Despite its unusual form, Eq. (17) produces curves similar to Gaussians, but with a skew that becomes more pronounced as α/L increases. α^2 roughly corresponds to the variance of the curve (and in the limit as L grows very large, Eq. (17) can be reduced to a Gaussian with SD, α). L represents the distance over which the linear dispersion coefficient changes by its magnitude at the focus point. α^2/L^2 determines the sharpness of the peak and is equal to the ratio of the characteristic focusing time scale, $1/E_0 \nu_0 f_1$ to the dispersion time scale, L^2/D.

This first-order model is the simplest model that captures the asymmetric tailing due to the axial variation in dispersion. Note that the solution breaks down at $\tilde{x} = -L$, and care must be taken in avoiding this unphysical range of the equation.

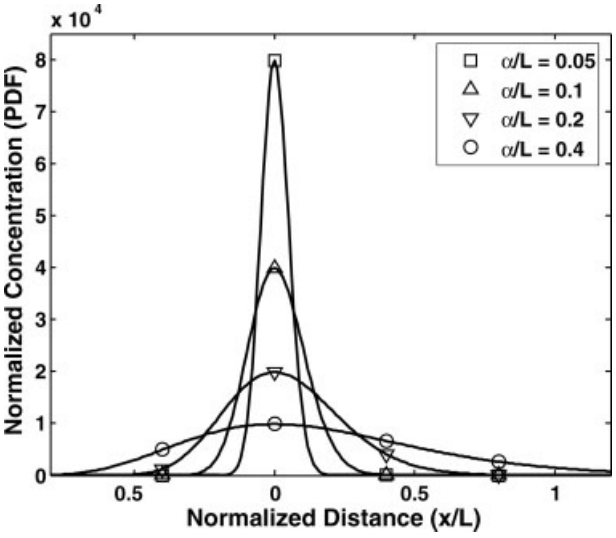

Figure 2. Nondimensional axial concentration profiles. This plot shows the effect of changes in the dispersion length scale, L, and focusing parameter, α, on steady-state concentration profiles. For large α/L, the peak is wider and strongly asymmetric. The concentration profiles are normalized to give equal areas under the curves.

4 Materials and methods

Our calibrations and experiments were performed with Tris-borate focusing buffer, composed of 900 mM Tris and 900 mM boric acid (Sigma-Aldrich, MO). The buffer conductivity and pH were measured with a combination pH/conductivity meter (Corning, NY). Conductivity ranged from 2.2 mS/cm at 20°C (σ_0) to 7.6 mS/cm at 74°C, while pH varied from 8.4 to 7.9 at 54°C. For temperature imaging and focusing experiments, we prepared solutions of rhodamine B (Arcos Organics, Belgium), fluorescein, Bodipy proprionic acid, and Oregon Green 488 carboxylic acid (Molecular Probes, OR) using in-house deionized water which was filtered with a 0.2 μm filter (Nalgene, NY) prior to use. We used 50 mm long rectangular borosilicate glass capillaries (Vitrocom, NJ) with nominal inner dimensions of 20 × 200 μm for our microchannels. The capillaries were mounted on a microscope slide or cover slip glass and encapsulated within polydimethyl siloxane (Sylgard 184, Dow Corning, MI, USA). Silicone O-rings were epoxied at the channel ends to interface to the external fluidics. The microchannel assembly is shown in Fig. 3.

4.1 Experimental setup

The microscope slide of the channel assembly was attached to two thermally regulated copper blocks using thermally conductive tape (3 M, St. Paul, MN) such that the capillary spanned a 2 mm gap between the blocks. The block temperature was controlled using thermoelectric heater/coolers (TE

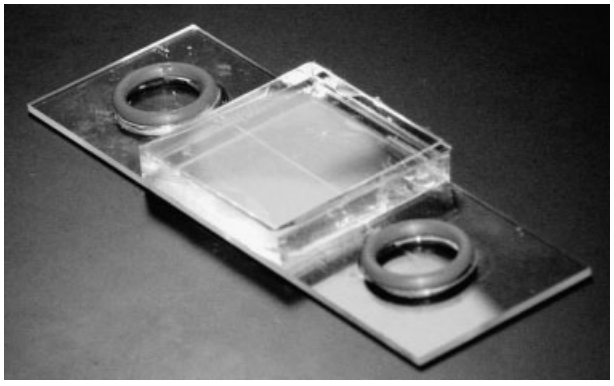

Figure 3. Microfluidic chip assembly. The 20×200 μm rectangular glass borosilicate capillary is just visible and spans the distance between two O-ring reservoirs and underneath an insulating PDMS block. As PDMS tended to adsorb dust and particles, a coverslip was adhered to the top of the PDMS block to provide an easily cleaned, and optically smooth upper viewing surface.

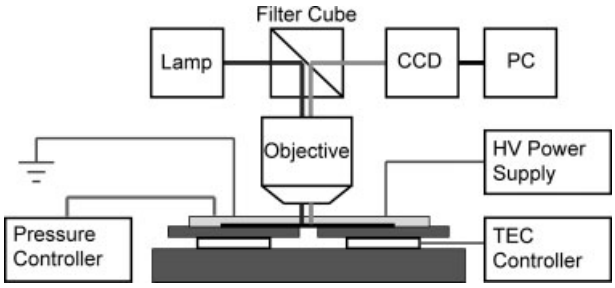

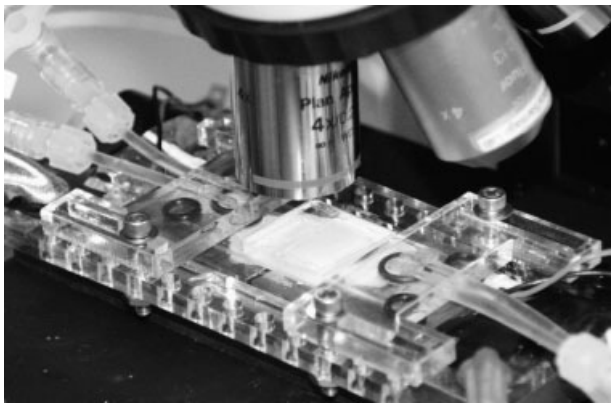

Figure 4. Control schematic and image of setup for TGF experiments. (a) The TGF assembly provides the thermal, fluidic, and electrical interface to the microchannel. A temperature gradient is established across a gap between two copper plates, each heated or cooled by a thermoelectric (Peltier) device. Pressure control is accomplished by adjusting the relative heights of two external reservoirs. (b) In the assembly photo, the microfluidic chip is mounted on the TGF assembly. The encapsulating PDMS block is located directly below the objective, and the fluidic manifolds are to the left and right of the block.

Technology) mounted on a copper, liquid-cooled, heat exchanger (Melcor, NJ). Water was circulated from an external reservoir by a miniature gear pump (Greylor Dynesco, FL). The temperature of each block was monitored using a thin film resistance temperature detector (RTD) (Omega Engineering, CT) and closed-loop control was provided by two TEC power supply/controllers (Alpha Omega Instruments, RI). A schematic for the experimental setup and a photo of the TGF fixture is given in Fig. 4.

For the temperature measurement and focusing experiments, a high-voltage power supply (Spellman, NY) provided up to 6000 V, giving a maximum applied field of 120 V/mm. We controlled the amount of externally applied pressure by adjusting the relative heights of two external reservoirs (two plastic 140 mL syringe barrels) using a Newport M-436 high-performance linear stage. The reservoirs were connected to the TGF assembly *via* large bore tubing (1/16th inch FEP tubing). In these experiments, current was measured using an Agilent 34001A digital multimeter (Agilent, CA), with a resolution of 0.5 μA. In all experiments, the potential was applied across the channel using platinum wire electrodes placed in the external reservoirs.

4.2 Current monitoring and conductivity measurement

We performed current monitoring experiments to quantify temperature-dependent electroosmotic mobility following the method described by Huang *et al.* [31]. Measurements were made in a TGF fixture with a single temperature-regulated block to present a uniform temperature to the capillary. To more accurately track the capillary temperature for the calibration measurements, we fabricated a microchannel assembly with a thin film RTD that was embedded within the PDMS block adjacent to the capillary. An Agilent 34970A Data Acquisition/Switch Unit (Agilent) measured the RTD output. A Keithley Sourcemeter 2410 (Keithley, OH) simultaneously applied voltages ranging from 100 to 1100 V and measured currents in approximately the 2–30 μA range. To measure the buffer conductivity *versus* temperature and thereby extract $f(T)$, we used the plateau current values from the current monitoring runs. These values agreed well with bulk conductivity measurements made using our conductivity meter.

4.3 Fluorescence imaging and temperature measurement

We performed fluorescence imaging using an upright epifluorescent microscope (Nikon) fitted with a $4\times$ objective with numerical aperture (NA) of 0.2 (Nikon). For the temperature calibration measurements, we used a $10\times$ objective with NA = 0.30. In both cases, images were subsequently reduced by a $0.5\times$ demagnifier before capturing on a cooled

12-bit interline CCD camera (Roper Scientific, AZ). The CCD featured a 1300 × 1024 pixel array and pixel size of 6.67 μm square. Illumination was provided by a mercury lamp filtered using a filter cube (Omega Optical) matched for the fluorophore under study. Neutral density filters (typically ND16 or ND4 × 16) were placed in the illumination train to reduce photobleaching-induced effects. Frame exposure times were 1000 ms for the focusing images and 250–300 ms for the temperature images. Fluorescence images were normalized using a correction of the form $NI = (S - B)/(F - B)$, where S is the raw image intensity, B the (illuminated) background, and F the flatfield intensity value. 1-D, area-averaged profiles were created by averaging pixel columns across the capillary.

We performed temperature field imaging based upon the temperature-dependent quantum efficiency of rhodamine B dye, using the method described by Ross and co-workers [8, 32]. Temperature measurements were performed in the focusing buffer. To construct the calibration curve for 100 μM rhodamine B in 900 mM Tris-borate buffer, we performed fluorescence measurements *versus* temperature using the single-block temperature-control fixture and microchannel assembly described in Section 4.2 [33, 34].

4.4 Focusing protocol

Focusing experiments were performed in the TGF assembly using 900 mM Tris-borate buffer. The system was configured with the left- and right-hand blocks as the cold and hot blocks, respectively. The magnitude and direction of applied pressure gradient varied according to the electric field, magnitude of the analyte's electrophoretic mobility, and the temperature conditions of the channel. In order to locate the initial peak, we loaded the dye into the left-side reservoir, then allowed the dye wave front to progress into the focusing volume under pressure-driven flow. Once the wave front was established, the applied voltage and pressure head were adjusted until focusing was observed.

For pseudo-steady measurements, we first allowed the sample peak to focus at constant rate until its relative growth rate, $\Delta c_0/c_0$, was negligible. Here Δc_0 is the change in the maximum concentration over the frame capture period (typically 15 or 30 s). In practice this meant that a negligible peak increase was observed between images taken 30 s apart. We then imaged the peak.

4.5 Velocity and diffusivity estimates

To quantify the amount of external pressure-driven flow, images of focused peak were recorded as the electrical circuit was opened (removing the imposed electric field and initiating a flow driven only by the height difference between the liquid levels in the reservoirs). By fitting Gaussians to the intensity profiles generated from the images of the moving peak, we estimated the area-averaged velocity by measuring the slope of the peak location *versus* time. To estimate the diffusivity, we performed a similar estimate, fitting peak variance with $\sigma(t)^2 = \sigma_0^2 + 2Dt$ following deactivation of the electric field.

5 Results and discussion

We performed a set of experiments to study TGF dispersion in practice and evaluate the range of applicability of the model.

5.1 Calibration results

The temperature field measurements verified the presence of a linear temperature gradient within the gap region for the focusing fields presented in this work. Figure 5 shows representative temperature profiles across the gap for a wide range of normalized electric fields. For this example, the left and right block temperatures were set to 20 and 60°C. The temperature gradient had to be corrected to account for temperature drops across the microchannel assembly. For example, at zero applied field, the buffer temperatures at the left and right sides of the gap were 27 and 54°C, respectively. For the electric field strengths used in this study, Joule heating effects were small (less than 3°C temperature rise at 50 V/mm) and transverse gradients were negligible (0.3°C or less difference across the channel width at 50 V/mm). Measured temperature profiles were fit using second-order polynomials. To estimate the temperature profiles at arbitrary fields, we used a 2-D interpolation matrix (*vs.* x and E).

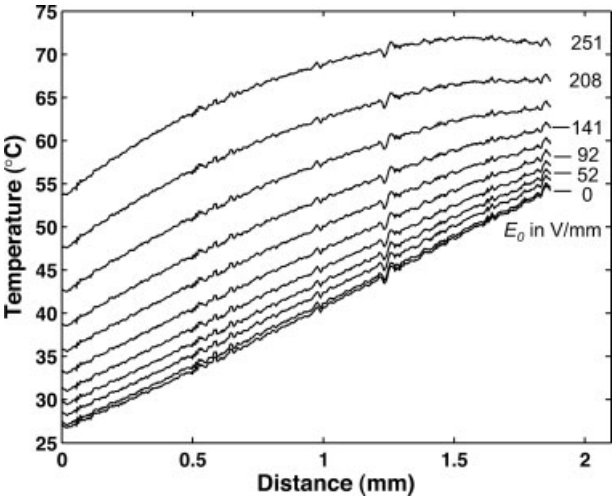

Figure 5. Sample axial temperature profiles *versus* reference field strength in a coverslip-based chip. Temperature profiles are shown for applied voltages of 0–5000 V at 500 V increments. The normalized electric field, E_0, is given for select profiles. The profiles span the distance between the regulating temperature blocks. The left block temperature was 20°C and right block temperature was 60°C. 1-D temperature profiles were generated from processed rhodamine B intensity images by averaging a 20 pixel strip (67 μm width) centered on the axis of the channel.

Using the results from 20 microchannel current monitoring measurements over the range of 10–80°C, we calculated $f(T)$, and found it to be in reasonable agreement with Ross and Locascio [8]. A least-squares fit using a cubic polynomial gives $f(T) = (-5.17E-7)T^3 + (1.17E-4)T^2 - (1.17E-2)T + 1.27$, with $R^2 = 0.998$. We also determined the electroosmotic mobility as a function of temperature, which was $\nu_{eo,0} = 1.1E-8$ m^2/V·s at the reference temperature (20°C). Using Eq. (3), we calculated $g(T)$, which was well described by a linear fit, $g(T) = 0.0047T + 0.91$ ($R^2 = 0.98$). By combining these functional forms of f and g with the temperature profile interpolation matrix, we could estimate the values of f, g, and f_1 (the slope for f linearized about the focus point) at arbitrary fields and locations.

Together, f, g, and the electroosmotic mobility allow the determination of the local slip velocity according to Eq. (3). Variations in f and g cause the local slip velocity to deviate from the axial mean, leading to internally generated pressure gradients [35]. The internally generated pressure flow and externally driven flow both contribute to advective dispersion (Eq. 12). In principle, it is possible to calculate the internally generated component of U_p using our lubrication solution, but in practice it is difficult because it depends not only on the temperature profile throughout the entire channel, but also on the temperature, geometry, and electroosmotic mobility of the external fluidic components. In our experiments, if we consider only the induced pressure flow due to temperature variation within the channel, the dominant contribution to U_p at the focus locations is the externally imposed flow velocity, while the magnitude of the internally generated pressure gradient is estimated to be less than 13% of U_p at the peak locations. We therefore chose to neglect internally generated pressure gradient flows in our subsequent dispersion calculations.

5.2 TGF results

To evaluate dispersion, we performed TGF experiments with a variety of fluorescent analytes, under a range of applied electric fields, $\Delta V/L_{ch}$, and nominal temperature gradients, $\Delta T/L_{ch}$. Figure 6 shows sample full-field fluorescence images of focused Bodipy proprionic acid with $\Delta T/L = 10$°C/mm and $\Delta V/L_{ch} = 10$–40 V/mm. The external pressure head, equal to the difference in fluid height between the two external reservoirs, increases roughly linearly, with -7 mm-H_2O applied for the 1 V/mm field and -25 mm-H_2O for 40 V/mm. The direction of electrophoretic flux is left to right, while the bulk flow is right to left, driven by electroosmosis. (Note the external pressure head in this case is acting to reduce the total bulk flow.)

For the focused peaks of Fig. 6, the temperature gradient is relatively small. Consequently, the change in diffusivity across the peak is also small. Under these conditions, the ratio of the peak width to the diffusivity-change length scale, α/L, is small and the area-averaged intensity profiles are nearly Gaussian in shape, as expected. In fact, under our experimental conditions, we found focused peaks are often well represented using Gaussians. Figure 7 shows a comparison between Gaussian and exponential-log fits to Bodipy focused in a larger temperature gradient, equal to 30°C/mm. For this data, we observe some skew. While the exponential-log solution better captures the tailing behavior, a Gaussian solution is also a very good approximation, and standard Gaussian fitting tools are useful in peak analysis. Based on these observations, we chose to measure our experimental peak widths using Gaussian fits.

To study peak width as a function of electric field, we performed a series of focusing experiments in approximately the same location. We used applied voltages of less than

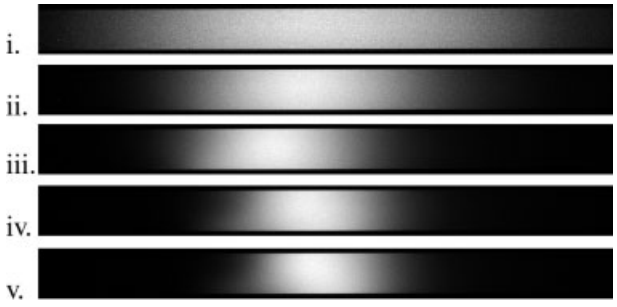

Figure 6. Full-field intensity images of focused Bodipy dye as a function of electric field strength. Images (i–v) show focused Bodipy dye within a 20×200 μm rectangular capillary. The applied temperature gradient was 10°C/mm and the applied electric fields ranged from -10 to -40 V/mm, yielding current-normalized fields, E_0, of (i) -1.5, (ii) -15, (iii) -30, (iv) -46, and (v) -64 V/mm. The net bulk flow is right to left, driven by electroosmosis.

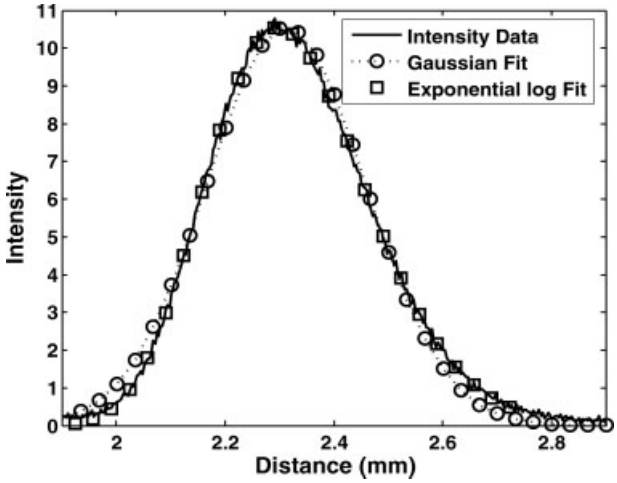

Figure 7. Comparison of Gaussian and skewed profiles. The plot compares fits using the Gaussian and exponential-log (or "skewed") solutions to the area-averaged intensity profile for a bodipy dye focused at an applied electric field, $\Delta V/L$, of 40 V/mm and an applied temperature gradient, $\Delta T/L$, of 60°C. The skewed solution better captures the profile asymmetry, but the Gaussian is a very good approximation.

2000 V to minimize the effects of Joule heating. The results are shown in the plot of Fig. 8. Here, the temperature regulating blocks were set at 20 and 40°C to give a near linear *f*-profile, and the mean focus temperature was 30.7°C with a SD of 1.1°C. The magnitude of the external pressure-driven velocity increased linearly from −0.6 to −62 μm/s with increasing field. The error bars show the 95% confidence interval based upon an error propagation estimate of the SD in focus position measured for the full data set. (The SD calculated from 15 frames of one realization is less than 0.5% of the measured width, indicating the accuracy of our pseudo-steady assumption.)

We see an approximately inverse square root dependence of peak width with respect to field. The field magnitudes of Fig. 8 correspond with an estimated Pe_a range of 0.01–1.2, based on our measurement of the externally driven pressure flow. Although we satisfy $Pe_a << L/a$ over the whole range, we violate our assumption that $P_w << L/w$ (for fields larger than 3 V/mm). Neglecting the additional ballistic dispersion incurred in the width dimension, Taylor dispersion (including the Chatwin modifier) is predicted to add about 20% over the molecular diffusivity, which corresponds to an increase in peak width of 10%. However, with this amount of advective dispersion, we expect to see greater curvature in our focused dye bands. Instead, the deviation is small (*i.e.*, $c' \approx 0$). We conclude that the internally generated and externally generated pressure gradients are counteracting one another, thus extending the applicability of the Taylor–Aris analysis.

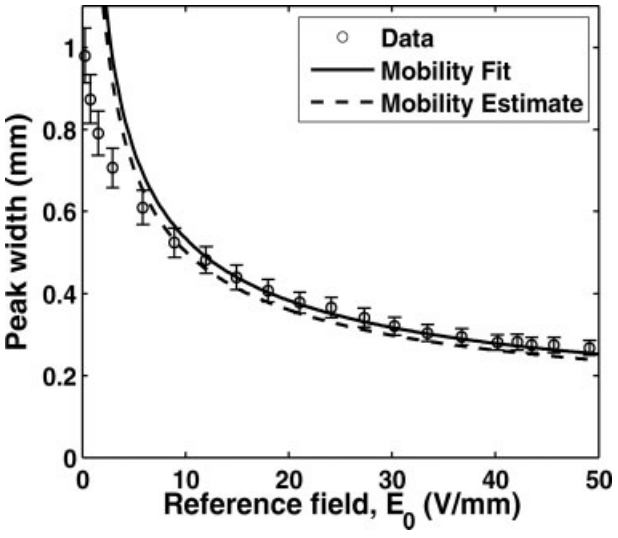

Figure 8. Bodipy peak width *versus* field. SDs are plotted for the Gaussian fit to the intensity profile data. Error bars show the 95% confidence interval of the peak width based on an error propagation analysis for the positional uncertainty of the full data set. The solid line shows the theoretical width prediction for a peak focused at the mean position, with $\nu_{eph,0} = -0.53E - 8\ m^2/V\cdot s$, $D_{foc} = 5E - 10\ m^2/s$, and f_1, = 34.5–31.4/m. The dashed line shows the theoretical prediction based on an independent mobility estimate of $\nu_{eph,0} = -0.6E - 8\ m^2/V\cdot s$.

Using the Gaussian solution, the theoretical peak width is $\alpha = \sqrt{-D_{foc}/E_0\nu_{eph,0}f_1}$. To generate predictions for the peak width, we assumed a uniform focus location equal to the mean position for the series for Figs. 6 and 8. The focus temperature (which ranged from 29.5 to 31.5°C) and f_1 (which decreased from −35 to −32/m with increasing voltage) were determined using the temperature interpolation matrix as a function of E_0, as described in Section 5.1. To determine the dispersion coefficient, we assumed U_p was negligible and set D_{foc} equal to the molecular diffusivity.

We needed to generate independent estimates of the diffusivity and electrophoretic mobility because the Bodipy proprionic acid interacted with the Tris buffer yielding multiple species (data not shown). For the diffusivity, we used the value obtained from our moving peak measurements (see Section 4.5), which was $D_{foc} = 5E - 10 \pm 1.5E - 10\ m^2/s$ at the mean temperature of 30°C. For the electrophoretic mobility we obtained two estimates. The first was generated from a fit of the experimental data (excluding the four lowest electric fields), giving $\nu_{eph,0} = -0.53E - 8\ m^2/V\cdot s$ and yielding the solid theory curve shown in Fig. 8. The second was an estimate derived from independent focusing measurements (data not shown), $\nu_{eph,0} = -0.6E - 8\ m^2/V\cdot s$, which gives the dashed curve of Fig. 8. (These values differ from published values for the electrophoretic mobility ($-2E - 8\ m^2/V\cdot s$) and diffusivity of Bodipy ($6E - 10\ m^2/s$) [36], which supports the hypothesis that the focused peak is not simply bodipy but a reaction product with the Tris buffer [37].)

The experimental and theoretical peak widths agree closely with some deviation at low fields. The low-field deviation falls below the line because the focused peak remains slightly "over-focused" as field was decreased, having had insufficient time to diffuse out to its "full" width. We are currently analyzing and constructing a model for TGF at higher fields. In our 10:1 aspect ratio channels, high field conditions correspond to $Pe_w > L/w$ and $Pe_a << L/a$. In such regimes, we expect both depth-wise Taylor dispersion and width-wise ballistic dispersion to be important, and we will report on this work in a future publication.

6 Concluding remarks

Maximizing resolution by minimizing dispersion is an important goal in most focusing techniques. In this work, we developed a generalized dispersion model to provide a framework for analyzing the various components that contribute to dispersion. We showed that dispersion is well modeled using an effective dispersion coefficient at low Peclet numbers and relatively low applied electric fields (below 400 V/cm for our particular setup). In this range, peak widths are well predicted by the focusing parameter, α.

In our experimental system (with its 10:1 aspect ratio channel cross-section), we found that, within the regime of applicability of our dispersion model, dispersion is well

approximated by diffusion alone. At higher fields, the assumption that $Pe_a << L/a$ and $Pe_w << L/w$ is violated. This will require the introduction of additional terms into the reduced deviation concentration Eq. (2). Additionally, at high field strengths, Joule heating can become appreciable and cause spanwise temperature gradients, requiring us to retain all the correlation terms in the mean transport Eq. (6). At such fields, our dispersion model fails and dispersion rate increases. In a future paper, we shall explore optimization of resolution across a wider range of electric fields, including the high field regime where the Taylor–Aris model fails and ballistic dispersion dominates.

This work was sponsored by the National Institutes of Health (grant N01-HV-28183) and an NSF PECASE Award (J. G. S., award number NSF CTS0239080) with Dr. Michael W. Plesniak as award monitor. D. E. H. was supported by a NDSEG Fellowship and ARCS Scholarship. We thank Rajiv Bharadwaj and Sumita Pennathur for helpful technical and motivational discussions related to this work.

7 References

[1] Reyes, D. R., Iossifidis, D., Auroux, P. A., Manz, A., *Anal. Chem.* 2002, *74*, 2623–2636.

[2] Auroux, P. A., Iossifidis, D., Reyes, D. R., Manz, A., *Anal. Chem.* 2002, *74*, 2637–2652.

[3] Vilkner, T., Janasek, D., Manz, A., *Anal. Chem.* 2004, *76*, 3373–3385.

[4] Yang, H., Chien, R. L., *J. Chromatogr. A* 2001, *924*, 155–163.

[5] Byoungsok, J., Bharadwaj, R., Santiago, J. G., *Electrophoresis* 2003, *24*, 3476–3483.

[6] Quirino, J. P., Terabe, S., *Science (Washington DC)* 1998, *282*, 465–468.

[7] Herr, A. E., Molho, J. I., Drouvalakis, K. A., Mikkelsen, J. C., Utz, P. J., Santiago, J. G., Kenny, T. W., *Anal. Chem.* 2003, *75*, 1180–1187.

[8] Ross, D., Locascio, L. E., *Anal. Chem.* 2002, *74*, 2556–2564.

[9] Ivory, C. F., *Sep. Sci. Technol.* 2000, *35*, 1777–1793.

[10] Bharadwaj, R., Santiago, J. G., Mohammadi, B., *Electrophoresis* 2002, *23*, 2729–2744.

[11] Bharadwaj, R., Santiago, J. G., *J. Fluid Mech.* 2005, *543*, 57–92.

[12] Taylor, G., *Proc. R. Soc. Lond. A* 1953, *219*, 186–203.

[13] Aris, R., *Proc. R. Soc. Lond. A* 1956, *235*, 67–77.

[14] Dutta, D., Leighton, D. T., *Anal. Chem.* 2002, *74*, 1007–1016.

[15] Brenner, H., *Langmuir* 1990, *6*, 1715–1724.

[16] Stone, H. A., Brenner, H., *Ind. Eng. Chem. Res.* 1999, *38*, 851–854.

[17] Griffiths, S. K., Nilson, R. H., *Anal. Chem.* 1999, *71*, 5522–5529.

[18] Pennathur, S., Santiago, J. G., *Anal. Chem.* 2005, *77*, 6772–6781.

[19] Balss, K. M., Ross, D., Begley, H. C., Olsen, K. G., Tarlov, M. J., *J. Am. Chem. Soc.* 2004, *126*, 13474–13479.

[20] Balss, K. M., Vreeland, W. N., Phinney, K. W., Ross, D., *Anal. Chem.* 2004, *76*, 7243–7249.

[21] Balss, K. M., Vreeland, W. N., Howell, P. B., Henry, A. C., Ross, D., *J. Am. Chem. Soc.* 2004, *126*, 1936–1937.

[22] Chen, C. H., Lin, H., Lele, S. K., Santiago, J. G., *J. Fluid Mech.* 2005, *524*, 263–303.

[23] Van Milligen, B. P., Bons, P. D., Carreras, B. A., Snchez, R., *Eur. J. Phys.* 2005, *26*, 913–925.

[24] Lin, H., Storey, B. D., Oddy, M. H., Chen, C.-H., Santiago, J. G., *Phys. Fluids* 2004, *16*, 1922–1935.

[25] Santiago, J., *Anal. Chem.* 2001, *73*, 2353–2365.

[26] Ghosal, S., *J. Fluid Mech.* 2002, *459*, 103–128.

[27] Ajdari, A., Bontoux, N., Stone, H. A., *Anal. Chem.* 2006, *78*, 387–392.

[28] Chatwin, P. C., Sullivan, P. J., *J. Fluid Mech.* 1982, *120*, 347–358.

[29] Dutta, D., Leighton, D. T., *Anal. Chem.* 2001, *73*, 504–513.

[30] Ghosal, S., Horek, J., *Anal. Chem.* 2005, *77*, 5380–5384.

[31] Huang, X. H., Gordon, M. J., Zare, R. N., *Anal. Chem.* 1988, *60*, 1837–1838.

[32] Ross, D., Gaitan, M., Locascio, L. E., *Anal. Chem.* 2001, *73*, 4117–4123.

[33] Huber, D., Santiago, J. G., *American Society of Mechanical Engineers, Fluids Engineering Division (Publication) FED* 2004, *260*, 263–266.

[34] Huber, D., Santiago, J. G., *J. Heat Trans. Trans. ASME* 2005, *127*, 806.

[35] Herr, A. E., Molho, J. I., Santiago, J. G., Mungal, M. G., Kenny, T. W., Garguilo, M. G., *Anal. Chem.* 2000, *72*, 1053–1057.

[36] Bharadwaj, R., Santiago, J. G., Mohammadi, B., *Electrophoresis* 2002, *23*, 2729–2744.

[37] Kemp, D. S., Vellaccio, F., *Organic Chemistry*, Worth Publishers, New York 1980.

[38] Anderson, J. L., Idol, W. K., *Chem. Eng. Commun.* 1985, *38*, 93–106.

[39] White, F. M., *Viscous Fluid Flow*, McGraw-Hill, Inc., New York 1991, p. 614.

Appendix A: Derivation of lubrication flow solution

For steady flows with $Re << 1$, we may eliminate the inertial terms yielding the Stokes equation. Analytical solutions exist for both the circular capillary [38] and parallel plate geometries [11]. Instead, we elect to use the lubrication theory approximation [39], which requires that $Re << L/a$. In practice, this means that the velocity field changes slowly over the length of interest. We can therefore neglect nonaxial velocities and solve for a "fully developed" flow profile at every location along the channel. Ghosal presents a mathemati-

cally rigorous development of the lubrication theory for microchannels with electroosmosis [26]. We extend the theory to account for temperature-based changes in the zeta potential, permittivity, viscosity, and electric field, abstracting these changes into the nondimensional f and g functions defined in Section 2. For our parallel plate geometry, this yields the local solution:

$$u_{\text{bulk}} = -\frac{a^2}{2\mu}\frac{\mathrm{d}p}{\mathrm{d}x}\left(1-\frac{y^2}{a^2}\right) + \nu_{\text{eo},0}E_0 fg \tag{A.1}$$

$$Q' = -\frac{2a^3}{3\mu}\frac{\mathrm{d}p}{\mathrm{d}x} + 2a\nu_{\text{eo},0}E_0 fg \tag{A.2}$$

where the new terms are $\mathrm{d}p/\mathrm{d}x$, the local pressure gradient and Q', the volumetric flow *per* unit depth. Here, the local pressure gradient is a function of both the applied external pressure and the internal pressure gradient generated by the varying electroosmotic slip velocity, while the volumetric flow rate is constant. Solving for the pressure gradient in terms of Q', we then integrate across the length of the channel to yield Q' in terms of the applied pressure ΔP:

$$Q' = \frac{2a^3}{3\langle\mu\rangle}\frac{\Delta P}{L} + 2a\nu_{\text{eo},0}E_0\frac{\langle\mu fg\rangle}{\langle\mu\rangle} \tag{A.3}$$

where the angled brackets indicate a axial average across the length of the channel, *e.g.*, $\langle f\rangle = (1/L_{\text{ch}})\int f\,\mathrm{d}x$. Equating Eqs. (A.2) and (A.3), we solve for the local pressure gradient:

$$\frac{\mathrm{d}p}{\mathrm{d}x} = -\frac{\mu}{\langle\mu\rangle}\frac{\Delta P}{L} + \frac{3\mu}{a^2}\nu_{\text{eo},0}E_0\left(fg - \frac{\langle\mu fg\rangle}{\langle\mu\rangle}\right) \tag{A.4}$$

Inserting Eq. (A.4) into Eq. (A.1) we now have the local bulk velocity profile as a function of $f(T)$ and $g(T)$.

$$u_{\text{bulk}}(x,y) = \left\{\frac{a^2}{2\langle\mu\rangle}\frac{\Delta P}{L} + \frac{3}{2}\nu_{\text{eo},0}E_0\left(\frac{\langle\mu fg\rangle}{\langle\mu\rangle} - fg\right)\right\}\left(1-\frac{y^2}{a^2}\right) + \nu_{\text{eo},0}E_0 fg \tag{A.5}$$

We then decompose the mean and deviation components to obtain

$$\bar{u}_{\text{bulk}} = \frac{a^2}{3\langle\mu\rangle}\frac{\Delta P}{L} + \nu_{\text{eo},0}E_0\frac{\langle\mu fg\rangle}{\langle\mu\rangle} \tag{A.6}$$

$$u'_{\text{bulk}} = \frac{U}{2}\left(1-\frac{3y^2}{a^2}\right) \tag{A.7}$$

where

$$U = \frac{a^2}{3\langle\mu\rangle}\frac{\Delta P}{L} + \left\{\nu_{\text{eo},0}E_0\frac{\langle\mu fg\rangle}{\langle\mu\rangle} - \nu_{\text{eo},0}E_0 fg\right\}$$

Here, U is the area-averaged value of the local pressure-driven flow, which includes the applied pressure component (left-hand term) and the internally generated component (bracketed terms).

One interesting insight produced by this derivation is that the mean electroosmotic velocity for the channel is determined not only by the axial mean of the zeta potential, permittivity, and field (which are captured in the product of E_0 and fg, see Section 2 for definitions), but also the viscosity. As a result, the mean EOF is the product of E_0 and the viscosity-weighted axial average of fg.

Appendix B: Scaling analysis

To begin our scaling analysis, we first expand the deviation concentration transport equation, Eq. (7), in its scalar form, eliminating off-axis velocity terms in accordance with the lubrication theory approximation (Appendix A):

$$\frac{\partial c'}{\partial t} + \bar{u}_{\text{bulk}}\frac{\partial c'}{\partial x} + u'_{\text{bulk}}\frac{\partial}{\partial x}(\bar{c}+c') + \frac{\partial \bar{u}_{\text{eph}}}{\partial x}c' + \\ + \bar{u}_{\text{eph}}\frac{\partial c'}{\partial x} - \frac{\partial c'}{\partial x}\frac{\partial \bar{D}}{\partial x} - c'\frac{\partial^2 \bar{D}}{\partial x^2} = \frac{\partial \bar{D}}{\partial x}\frac{\partial c'}{\partial x} + \\ + \bar{D}\frac{\partial^2 c'}{\partial x^2} + \bar{D}\frac{\partial^2 c'}{\partial y^2} + \frac{\partial}{\partial x}\overline{u'_{\text{bulk}}c'} \tag{B.1}$$

Next we nondimensionalize using the following scales,

$$\hat{t} = \frac{t}{\tau_{\text{foc}}}, \quad \hat{c}' = \frac{c'}{C'}, \quad \hat{\bar{c}} = \frac{\bar{c}}{\bar{C}}, \quad \hat{\bar{u}}_{\text{bulk}} = \frac{\bar{u}_{\text{bulk}}}{U_{\text{bulk}}},$$
$$\hat{u}'_{\text{bulk}} = \frac{u'_{\text{bulk}}}{U_{\text{p}}}, \quad \hat{\bar{u}}_{\text{eph}} = \frac{\bar{u}_{\text{eph}}}{U_{\text{eph}}}, \quad \hat{\bar{D}} = \frac{\bar{D}}{D_0}$$
$$\hat{x}_{\text{vel,diff}} = \frac{x}{L_{\text{grad}}}, \quad \hat{x}_{\text{conc}} = \frac{x}{L_{\text{peak}}}, \quad \hat{y} = \frac{y}{a} \tag{B.2}$$

where τ_{foc} is the characteristic focusing time scale, C' the characteristic deviation concentration, $\bar{C}$ the characteristic mean concentration, U_{bulk} the mean bulk velocity, and U_{eph} the electrophoretic velocity at the focus point (remaining terms are as defined in the main text of the paper). We note that there are two characteristic length scales in the axial direction. The disparate scales arise because the velocity and diffusion terms vary over the length of the temperature gradient, L_{grad}, while the concentration terms vary over the length of the focused peak, L_{peak}. The subscripts on $\hat{x}$ indicate the derivatives for which the scalings apply. After substitution, we have

$$\left(\frac{a^2}{\tau_{\text{foc}}D_0}\right)\frac{\partial c'}{\partial t} + \left(\delta\frac{U_{\text{bulk}}}{U_{\text{p}}}\right)\bar{u}_{\text{bulk}}\frac{\partial c'}{\partial x} + \left(\delta\frac{\bar{C}}{C'}\right)u'_{\text{bulk}}\frac{\partial \bar{c}}{\partial x} + \\ + (\delta)u'_{\text{bulk}}\frac{\partial c'}{\partial x} + \left(\delta\frac{L_{\text{peak}}}{L_{\text{grad}}}\frac{U_{\text{eph}}}{U_{\text{p}}}\right)\frac{\partial \bar{u}_{\text{eph}}}{\partial x}c' + \left(\delta\frac{U_{\text{eph}}}{U_{\text{p}}}\right)\bar{u}_{\text{eph}}\frac{\partial c'}{\partial x} - \\ -\left(\frac{a^2}{L_{\text{grad}}L_{\text{peak}}}\right)\frac{\partial c'}{\partial x}\frac{\partial \bar{D}}{\partial x} - \left(\frac{a^2}{L_{\text{grad}}^2}\right)c'\frac{\partial^2 \bar{D}}{\partial x^2} = \left(\frac{a^2}{L_{\text{grad}}L_{\text{peak}}}\right) \\ \frac{\partial \bar{D}}{\partial x}\frac{\partial c'}{\partial x} + \left(\frac{a^2}{L_{\text{peak}}^2}\right)\bar{D}\frac{\partial^2 c'}{\partial x^2} + (1)\bar{D}\frac{\partial^2 c'}{\partial y^2} + (\delta)\frac{\partial}{\partial x}\overline{u'_{\text{bulk}}c'} \tag{B.3}$$

where we have eliminated the carats on the nondimensional variables for clarity. δ is our smallness parameter, and the

terms in parentheses are the nondimensional parameters for our scaling. Since we are considering dispersion in the Taylor–Aris regime, the Taylor dispersion criterion, $L_{peak}/a \gg Pe_a$, holds, and we have substituted for $\delta = (a/L_{peak})Pe_a$.

We wish to simplify the equation and produce a form that gives an explicit solution for c'. In our system the characteristic velocities have the same order of magnitude, since they are linked through the focusing criterion. The axial lengths are much longer than the channel depth ($L_{grad} \cdot L_{peak} \gg a$), and, under the Taylor–Aris regime, $c' \ll \bar{c}$. Therefore, we can substitute δ for a/L_{peak}, a/L_{grad}, and $c'/\bar{c}$. Eliminating all terms of order δ or higher, we get

$$\left(\frac{a^2}{\tau_{foc} D_0}\right)\frac{\partial c'}{\partial t} + u'_{bulk}\frac{\partial \bar{c}}{\partial x} = \bar{D}\frac{\partial^2 c'}{\partial y^2} \qquad \text{B.4}$$

Considering the characteristic time scale, we note that for times on the order of the diffusive time scale ($\tau_{diff} = a^2/D_0$), the deviation concentration is unsteady. However, we are interested in times on the order of the focus time, which is given by the ratio of the focusing distance to the net focusing velocity. (For the case of a linear gradient of f, this gave $\tau_{foc} = L_{peak}/E_0 \nu_{eph,0} f_1 L_{peak}$.) To eliminate the unsteady term, we require one additional scaling argument, which is

$$\tau_{foc} \gg \tau_{diff} \equiv \frac{a^2}{D_0} \qquad \text{B.5}$$

However, recognizing that the width of the peak, $L^2_{peak} \sim D_0 \tau_{foc}$, substituting above, we see that our focus time requirement is already met by our scaling assumption that $a << L_{peak}$. Equation (B.4) can now be reduced to Eq. (9) and solved for c', as described in the main text.

